THE JOURNAL OF PHYSICAL CHEMISTRY C
A JOURNAL OF THE AMERICAN CHEMICAL SOCIETY

pubs.acs.org/JPCC

Article

Direct Observation of Intermediates from the Ring-Opening of Cetylpyridinium Chloride by Surface-Enhanced Raman Spectroscopy

Gen Liu, Danni Hao, Kai Wang, Gang Dong, Xue Yu, Rui Xu, Mei Ji, Xiaodong Zhu, Yanqing Ma,* and Lei Ma*

Cite This: J. Phys. Chem. C 2021, 125, 18792−18798

Read Online

ACCESS | Metrics & More | Article Recommendations | Supporting Information

ABSTRACT: The carbonization of pyridine is often observed in surface-enhanced Raman spectroscopy (SERS) measurements, while the potential ring-opening process and reaction mechanism remain elusive. In this paper, pyridine derivative cetylpyridinium chloride was chosen as a model molecule; its ring-opening process was captured and monitored through the technique of in situ SERS. The results show that if pyridyl and pyridyne are produced first, then the reaction route of *m*-pyridyl is *m*-Pyridyl →*2,3*- and *3,4*-Pyridyne →*m*-TS1 →*m*-IM1 →*m*-TS4 →*m*-IM3 (*m*-TS1, *m*-IM1, *m*-TS4, and *m*-IM3 are the products of *m*-pyridyl; IM: intermediate; TS: transition states), which perfectly matches the theoretically predicted lowest energy cost path and can be interpreted, as the surface plasmonic resonance of Au nanoparticles promoted the reaction. SERS and XPS measurements indicate that the reaction occurred at certain sites with the strongest enhanced electric field according to the Finite difference time domain calculation. These results prove the applicability of SERS in the in situ study of high-energy cost reaction and further expand its application in in situ detection of chemical reaction processes in general.

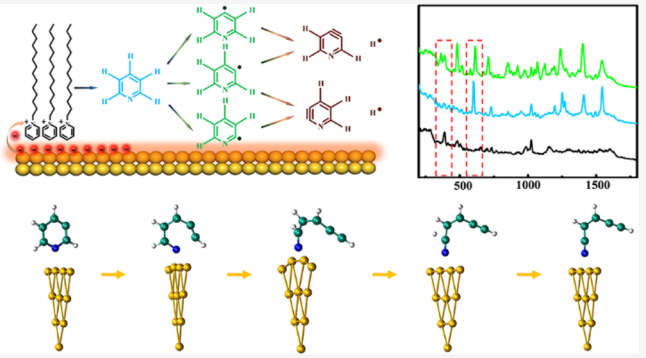

INTRODUCTION

As an important intermediate of the coal and petrochemical industry, pyridine and its derivatives have attracted great attention for many decades.[1−4] It is obvious that completely elucidating the mechanism of the pyridine cleavage will open an avenue for developing highly efficient catalysts. However, due to the presence of a remarkably stable N-heterocyclic ring, pyridine cleavage under mild conditions is extremely challenging, and only a very few well-defined heterogeneous catalysts have been found,[2−5] which makes it is very hard to identify of the reaction intermediates and clarify the reaction pathways.

The important intermediates of the pyridine ring-opening reaction are pyridine radicals, such as *o*-, *m*- and *p*-pyridyl radicals; they can be formed by loss of one hydrogen atom from pyridine and have been observed by using electron spin resonance spectroscopy (ESR) and neutralization-reionization mass spectrometry.[6−8] Loss of two hydrogen atoms resulted in formation of 3,4- and 3,5-pyridyne, which were observed by Nam and Winkler et al. through matrix isolation infrared spectroscopy study of UV photolysis products of 3,4-pyridine dicarboxylic acid and vacuum pyrolysis of 3,5-diiopyridine, respectively.[9,10] For the Ca−pyridine system, the involvement of the ring-opening of 2,3- and 3,4-pyridyne has been confirmed based on the Raman measurements.[5] This also indicates the strong yielding preference of pyridyne as the product of ring-opening. Additionally, the absolute enthalpies of 2,3-, 2,4-, and 3,4-pyridyne formation have been experimentally measured by Rau et al.[11] The degradation products of the ring-opening reaction after the formation of these radicals were also identified by electrospray ionization mass spectrometry, IR spectroscopy, and ESR.[6,10,12] Several theoretical predictions on the reaction route were reported.[13−19] Furthermore, LaVerne et al.[15] calculated the vibration frequency of pyridyl radicals in detail; Cheng et al. predicted a series of ring-opening products and corresponding vibration frequencies arising from *o*-, *m*-, and *p*-pyridyl radicals.[16−18] However, high-energy requirement of ring-opening reactions and their intrinsic weak spectral signals of products largely limit the in situ detection and monitoring. Both locally concentrated high-energy and surface-enhanced Raman spectroscopy (SERS) characteristics of surface plasmonic resonance (LSPR) in plasmonic metallic nanostructures make the detection of the intermediates possible.

Received: April 27, 2021
Revised: August 11, 2021
Published: August 19, 2021

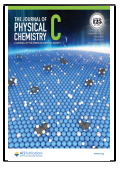

https://doi.org/10.1021/acs.jpcc.1c03760
J. Phys. Chem. C 2021, 125, 18792−18798

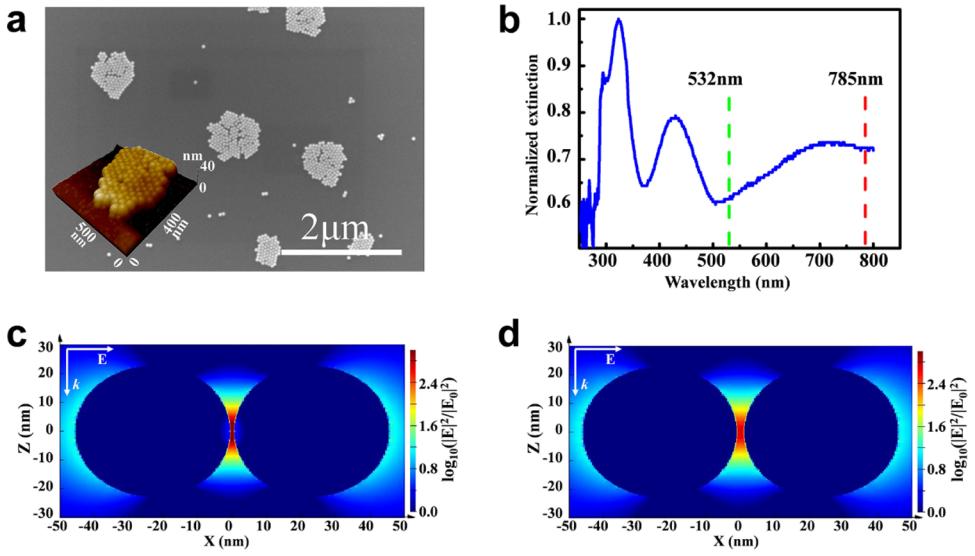

Figure 1. (a) SEM image of self-assembled Au NPs on ITO glass; the inset image in (a) shows the AFM image of the sample; (b) extinction curve of the SERS platform. Finite difference time domain simulations were employed to compute the local near field intensities in a system consisting of two nanospheres (diameter of 45 nm) with gap of (c) 1 nm and (d) 2 nm.

The LSPR is the collective oscillation of free electrons in plasmonic metal. When metallic nanostructures are irritated by light, the hot carriers, enhancement field, and thermal effect resulting from the LSPR effect all possibly contribute to the catalysis reaction and open new reaction pathways due to the reduction of the reaction barrier.[20−24] Additionally, the LSPR-resulted SERS signals could be enhanced by a factor of ∼10^6−10^{12}, compared to the signals from conventional Raman spectroscopy measurements, which leads to the detection of single molecules being reachable.[25,26] This also indicates the possibility of employing Raman spectroscopy to identify reaction routes.[27−30] Pyridine being the first molecule studied by SERS, its adsorption and SERS enhancement on plasmonic metal have been intensively investigated.[26,31,32] For instance, Tian et al.[32] reported an extraordinary enhancement of Raman scattering from pyridine on single-crystal Au and Pt electrodes by shell-isolated Au nanoparticles. There, its average enhancement reaches 10^6 for Au (110) and 10^5 for Pt (110). Meanwhile, the carbonization of pyridine is often observed in SERS measurements. Originally, it was attributed to laser carbonization, while with better understanding of the catalytic effect of the plasmonic metal, people started to realize that the carbonization more likely resulted from the plasmonic metal.[27,33] However, reports on plasmonic metal catalysis of the pyridine ring-opening reaction are rare. This is mainly due to the fact that (1) plasmonic metal-induced reaction pathways actually highly depend on their reaction environment and (2) a broad spectrum of products in ring-opening reactions, which make elucidation of the reaction mechanism extremely difficult.[27] Recently, a plasmon-mediated intramolecular methyl migration reaction of *N*-methylpyridinium to 4-methylpyridinef was reported; the Au film deposited on a nanosphere-covered substrate is useful for both reaction induction and process characterization.[34] It highlights the capability of plasmonic metal to drive complex and selective reactions.

In this work, as a SERS platform, a self-assembled Au NP−cetylpyridinium chloride (CPC) system is fabricated. The quasi-dynamic ring-opening processes of pyridine were monitored through in situ Raman spectra in different medium environments, including water, air, Ar, and N_2. The reaction routes and catalysis mechanism are explored through the measured SERS signals. This provides significant references for further unveiling the catalytic properties of plasmonic NPs and the reaction mechanism of pyridine molecules.

RESULTS AND DISCUSSION

SERS Platform. SERS platforms consisting of Au NP (∼45 nm) monolayers on different substrates are prepared, as shown in Figure 1a and Figure S3. More details of material self-assembly are shown in the Supporting Information. Since the total number of aggregated nanoparticles within each group varies, they could have different plasmonic resonance frequencies.[35,36] A key feature of LSPR is the production of the extinction cross sections tens of times larger than the geometric cross section of a single nanoparticle (according to Mie approximation, a sphere NP's extinction cross section (σ_{ext}) is $\sim\frac{\varepsilon_2}{[\varepsilon_1+2\varepsilon_m]^2+\varepsilon_2^2}$; ε_1 is the real part of the dielectric function and describes the polarizability of metals relative to wavelength; ε_2 is the imaginary part of a dielectric function, directly related to photon absorption at a specific wavelength; and ε_m is the dielectric constant of the medium).[37,38] Figure 1b shows the normalized UV−vis extinction spectrum of the Au SERS platform; it exhibits a broad extinction band from 500 to 800 nm. The dotted lines indicate the Raman laser wavelengths of 532 nm (green) and 785 nm (red). In order to avoid exciting the interband transitions of Au, a 785 nm laser was chosen as the excitation laser for Raman measurements. Finite difference time domain (FDTD)-based simulations were conducted to calculate the local electric field intensity distribution of a model system for SERS platforms. The results are shown in Figure 1c,d, Figures S4, and S5 and indicate that the strongest electric fields are generated in hot spots. The resulting enhanced field is more than three orders of magnitude higher than the incident electric field of light ($(|E|/|E_0|)^2 \sim 3 \times 10^3$). This invokes that the capability of Au SERS platforms to be used for exciting LSPR and generate a locally enhanced field with a 785 nm laser. However, the exact field intensity at each site could not be implicitly determined

https://doi.org/10.1021/acs.jpcc.1c03760
J. Phys. Chem. C 2021, 125, 18792−18798

because of the variation of the number of particles and interparticle gaps in each aggregation site. Additionally, the contributions of quantum tunneling cannot be ignored when the particle−particle gap is less than 0.5 nm, since it can unavoidably cause a notable blue shift of the LSPR peak and further reduce the strength of the electromagnetic field.[39] Although this calculation can only be used to qualitatively evaluate the field strength, it is adequate to demonstrate locations of enhanced field.

Raman Signal of the SERS Platform. The CPC molecule is the most commonly used pyridine surfactant. Normally, its pyridine head stands on the metal surface of the substrate, and the alkyl chain is away from the substrate as reported in previous SERS studies.[40−42] However, much less is known about the ring-opening of its N-heterocycle head. Figure S6 shows the Raman spectrum of CPC powder measured in air using the 785 nm laser with the maximized output of laser intensity of 100 mW cm^{-2}. In the measured spectrum, the head group corresponds to the in-plane ring deformation vibration band at ∼646 cm^{-1}, the symmetrical and trigonal ring breathing mode band at ∼1029 cm^{-1}, the ring stretching vibration band at ∼1636 cm^{-1}, and the CH ring stretching mode band at ∼3084 cm^{-1}. The vibration of the long tail chain corresponds to the bands located at ∼1061, ∼1130, ∼1298, ∼1445, ∼1469, ∼2853, and ∼2880 cm^{-1}.[40−42] No significant peak changes and new peak appearance indicate no laser carbonization of CPC molecules; this further rules out the possibility of laser carbonization in following tests when a much lower laser intensity of 16 mW cm^{-2} is applied.

Figure 2a shows the Raman spectra of the Au−CPC system with a 785 nm laser and 300 s integration time. The

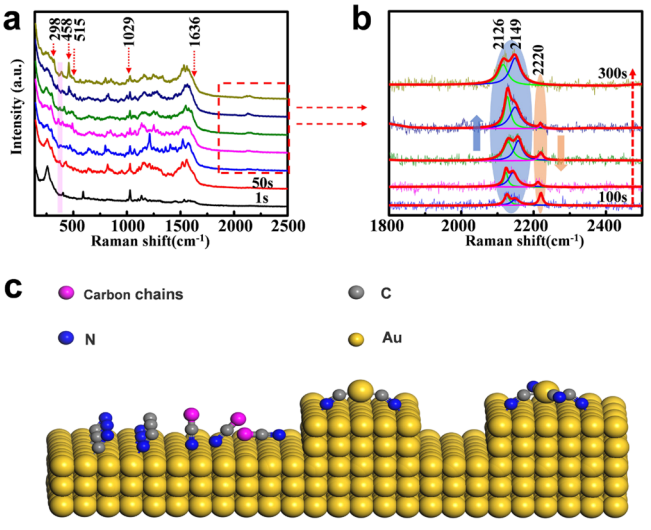

Figure 2. (a) Change of the SERS signal of the Au−CPC systems during the first 300 s; (b) detailed spectrum of the red dashed square enclosed part inside (a) with fittings; (c) schematic diagram of Au−CN with different bonding orientations.

appearance of abundant new peaks indicates the formation of new products. More detailed information of the reaction process will be discussed in the next section.

Figure 2b shows a group of new peaks between 2100 and 2225 cm^{-1}; they can be assigned to the vibration modes of C≡N and C≡C. Due to the instability of C≡C, the following discussion will mainly concentrate on C≡N bonds. As shown in Figure 2b, peaks at ∼2126, ∼2149, and ∼2220 cm^{-1} are mainly attributed to the different orientations and bond formation of C≡N on the Au NP surface. The previously reported SERS peaks of Au−CN have been summarized in Table S1 and Figure 2c, including free CN, $[Au(CN)_2]^-$, $[Au(CN)_4]^-$, Au−CN, and Au−NC. The binding of CN to Au is similar to that of S, which derives from the Au (111) undergoing the 23 $\times\sqrt{23}$ herringbone reconstruction with an adatom binding two CN^- (S_2^-) with the lowest energy cost.[43] Molecular orbital calculation suggests the formation of $[Au(CN)_2]^-$ and $[Au(CN)_4]^-$ mainly through orbital mixing of Au, which shows the characteristics of the *s* orbital and the corresponding adsorption features.[44] Recent studies have proposed that the 5*s* and 2*p** molecular frontier orbitals of n-CN interact with metal and produce *s-d* donation and *d-p** back-donation, respectively.[45] A weaker *s-d* interaction or a stronger *d-p** interaction would blue-shift the Raman frequency of n-CN. For Au−CN, LSPR effect provides large amounts of free electrons to the 2*p** orbital of n-CN, leading to a stronger *d-p** interaction that consequently shifts the frequency of CN to a higher wavenumber. This is well consistent with the fact of CN peak shift from ∼2137 to ∼2227 cm^{-1}. After cleaning the sample with Ar/H_2 plasma, only the molecules with the strongest bonds will be left (as shown in Figure S7). Figure 2b shows, at 100 s, a prominent peak at 2220 cm^{-1}, indicating that the initial CN is closer to the nanoparticles. With the increase of time, the ∼2220 cm^{-1} peak gradually disappears, while the peak at ∼2149 cm^{-1} significantly increases and shifts to ∼2126 cm^{-1}, indicating relatively weaker *d-p** back-donation.[45] The low wavenumber regime also shows peaks at ∼298 cm^{-1} (δ(Au−C≡N)), ∼370−390 cm^{-1} (ν(Au−CN)), ∼458 cm^{-1} (ν(Au−CN): CN parallel to the surface), ∼515 cm^{-1} (ν(Au−CN): CN bent toward the surface), and ∼530 cm^{-1} (ν(Au−CN): CN parallel to the surface). The two peaks in the XPS curve of N1s correspond to different adsorption forms on the surface of Au NPs,[46] as shown in Figure S8a. A significant peak shift occurs from ∼401.5 to ∼402.2 eV after the reaction; the catalysis could include multicontributions of the LSPR effects, and the possible reaction pathways will be discussed below. Meanwhile, the interference resulting from the evaporated Au film is excluded due to the fact that it was deposited under a pressure of 6.6×10^{-4} Pa and could rarely introduce N or other purities, as shown in Figure S8b.

Discussion of Reaction Routes. Figure S9a−c shows the SERS spectra of the sample in the first 60 s in air, which clearly show a periodic change. Figure S9d−f provides a change process of peak intensity from 0 to 300 s, including the Raman shift from 100 to 2500 cm^{-1}. There are clear trends for the peak at ∼480 cm^{-1} (from appearing, enhancing to decreasing), ∼1024 cm^{-1} (always existing), and ∼2130 cm^{-1} (from appearing to enhancing). Assignments of these bands are summarized in Figures 3 and 4 and Tables S2−S5. Figure 3a shows the SERS spectra measured at 2 and 10 s. Many new peaks appeared at 10 s. Among them, the most prominent peak is the one at ∼601 cm^{-1}, which is attributed to $\delta(ring)_{ip}$ of pyridine.[5,19] The peaks at ∼332 cm^{-1} and ∼1051(and ∼1072) cm^{-1} are attributed to $\delta(ring)_{oop}$ and $\delta(C-H)_{ip}$ of pyridine, respectively.[5,19] Other peaks of pyridine are summarized in Table S2. The transformation from CPC to pyridine is observed. The adsorbed CPC^+ molecule is a strong electron acceptor, which will be strongly targeted by the large amount of high-energy hot electrons yielded from LSPR, resulting in the bond breaking and loss of the alkyl chain.[34] When the

https://doi.org/10.1021/acs.jpcc.1c03760
J. Phys. Chem. C 2021, 125, 18792−18798

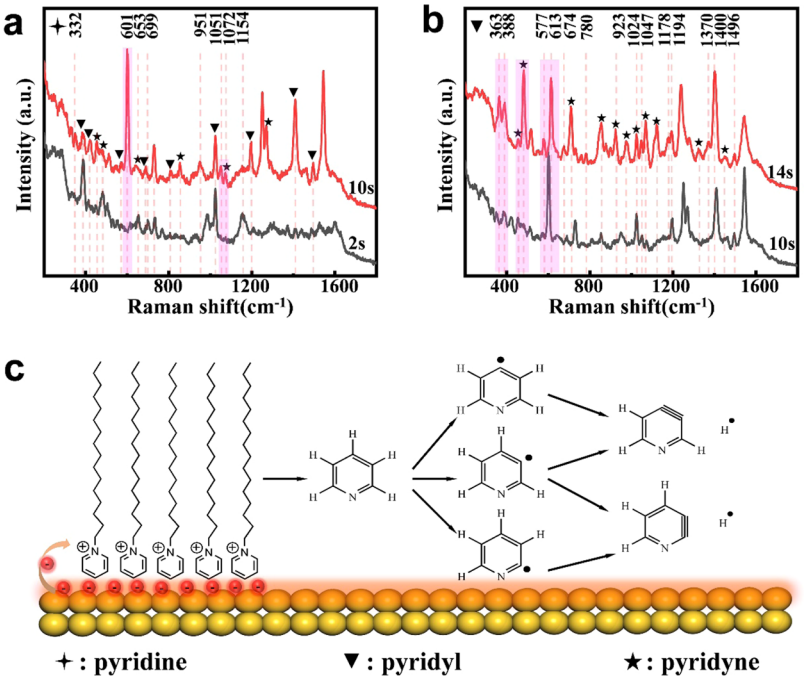

Figure 3. SERS spectra of CPC at (a) 2 and 10 s; (b) 10 and 14 s; and the (c) corresponding molecular structures of reaction products. The peaks and their corresponding chemical molecules and vibration modes are summarized in Table S2.

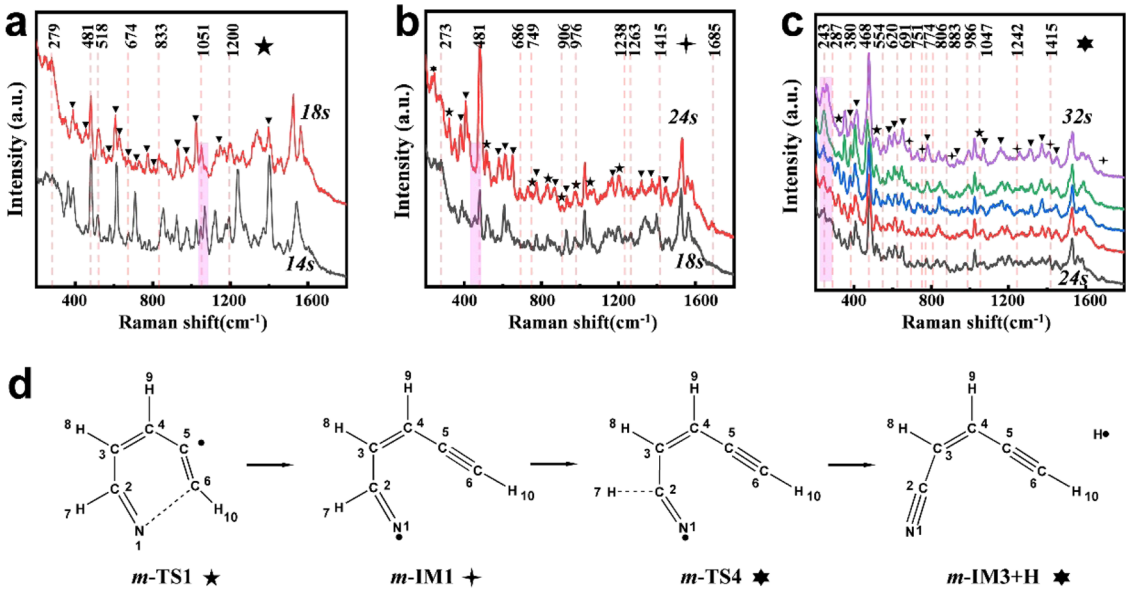

Figure 4. SERS spectra of CPC at (a) 14 and 18 s; (b) 18 and 24 s; (c) 24 and 32 s; and the (d) corresponding molecular structures of reaction products in the reaction pathway. The black solid inverted triangle represents the peaks of pyridyl and pyridine. Peaks and their corresponding chemical molecules and vibration modes are summarized in Tables S3 and S4.

reaction runs from 10 to 14 s, the peak at ~332 cm^{-1} disappears. Simultaneously, the peaks at ~363 and ~388 cm^{-1} appear, the intensity increases, and the peak at ~601 cm^{-1} starts to split into two peaks at ~577 and ~613 cm^{-1}, respectively, as shown in Figure 3b. *o-*, *m-*, and *p*-Pyridyl radicals have two Raman active vibrations modes of $\delta(\text{mol})_{oop}$ and $\delta(\text{ring})_{ip}$ corresponding to the peaks at 377 and 572 cm^{-1}, 381 and 572 cm^{-1}, and 370 and 612 cm^{-1}.[16−18] However, those peaks appearing at ~674, ~780, ~1024, ~1178, ~1400, and ~1496 cm^{-1} are attributed to the *m*-pyridyl radical: they are $\delta(\text{C−H})_{oop}$ (674 cm^{-1}), $\delta(\text{ring})_{oop}$ (770 cm^{-1}), $\delta(\text{C−H})_{ip}$ (1024 cm^{-1}), $\delta(\text{C−H})_{ip}$ (1177 cm^{-1}), δ(C−H) (1407 cm^{-1}), and $\delta(\text{C−H})_{ip}$ (1495 cm^{-1}).[18] The peaks at ~1047, ~1370, and ~1496 cm^{-1} are consistent with those for the *p*-pyridyl radical of $\delta(\text{C−H})_{ip}$ (1045 cm^{-1}), δ(C−H) (1377 cm^{-1}), and $\delta(\text{C−H})_{ip}$ (1491 cm^{-1}) cm^{-1}, respectively.[17] Therefore, there are mainly *m*-pyridyl and *p*-pyridyl in the reaction. It is also important to note that there are peaks at ~453 and ~481 cm^{-1} in Figure 3b, which could be assigned to the $\delta(\text{C}{\equiv}\text{C})_{ip}$ (451 cm^{-1}) and $\delta(\text{C}{\equiv}\text{C})_{oop}$ (478 cm^{-1}) of 3,4-pyridyne, respectively.[5,16−18] The peaks at ~407, ~453, ~481, ~627, ~854, ~1169, ~1238, ~1400, and ~1461 cm^{-1} could be assigned to the 3,4-pyridyne of $\delta(\text{mol})_{oop}$ (403 cm^{-1}), $\delta(\text{C−C})_{ip}$ (451 cm^{-1}), $\delta(\text{C−C})_{oop}$ (478 cm^{-1}), δ(mol) (637 cm^{-1}),

https://doi.org/10.1021/acs.jpcc.1c03760
J. Phys. Chem. C 2021, 125, 18792−18798

δ(N−C−C) (848 cm^{-1}), $\delta(C-H)_{ip}$ (1169 cm^{-1}), $\delta(C-H)_{ip}$ (1247 cm^{-1}), δ(mol) (1397 cm^{-1}), and δ(C−H) (1457 cm^{-1}), respectively. Also, peaks at ∼407, ∼709, ∼930, ∼972, ∼1024, ∼1129, ∼1150, and ∼1446 cm^{-1} could be assigned to 2,3-pyridyne of δ(mol)oop (411 cm^{-1}), $\delta(mol)_{ip}$(712 cm^{-1}), δ(H−C−C−C−H) (926 cm^{-1}), δ(H−C−C−H) (972 cm^{-1}), δ(H−C−C−C−H) (1025 cm^{-1}), δ(H−C−C−H) (1134 cm^{-1}), δ(H−C−C−H) (1156 cm^{-1}), and $\delta(H-C-C-H)_{ip}$ (1445 cm^{-1}), respectively. As a result, the reaction produces not only *o*-, *m*-, and *p*-pyridyl but also 2,3- and 3,4-pyridyne. The relevant vibration modes are summarized in Table S2, and the corresponding molecular structures are schematically shown in Figure 3c.

As the reaction proceeded, the peaks at ∼1047 and ∼1068 cm^{-1} shifted to ∼1051 cm^{-1} from 14 to 18 s, as shown in Figure 4a. It can be assigned to the δ(mol) of *m*-TS1. At the same time, there were obvious strong peaks at ∼279, ∼321, ∼481, ∼518, and ∼833 cm^{-1}, which were found to be related to *m*-TS1: δ(mol) (280 cm^{-1}), $\delta(mol)_{oop}$ (319 cm^{-1}), $\delta(H-C-C-C-H)_{oop}$ (479 cm^{-1}), $\delta(ring)_{ip}$ (515 cm^{-1}), and δ(ring) (835 cm^{-1}).[18] The peaks at ∼453 cm^{-1} disappeared from 18 to 24 s, as shown in Figure 4b; the peaks at ∼453 cm^{-1} could include the peak at 451 ($\delta(C-C)_{ip}$) cm^{-1} of 3,4-pyridyne and i442 (ν(N−C)) $cm^{-1}$of *m*-TS1.[17,18] The peaks at ∼279 cm^{-1} gradually shifted to ∼273 cm^{-1}; it can be assigned to the $\delta(mol)_{ip}$ (271 cm^{-1}) of *m*-IM1; and the peaks at ∼481 cm^{-1} further enhanced resulting from the products of *m*-IM1 having the vibration model δ(C−C−C−C) (486 cm^{-1}) and $\delta(mol)_{oop}$ (487 cm^{-1}). Meanwhile, the new peaks at ∼686, ∼1238, ∼1263, ∼1415, and ∼1685 cm^{-1} could be assigned to *m*-IM1: $\delta(C-H)_{ip}$ (679 cm^{-1}) and $\delta(C-H)_{ip}$ (681 cm^{-1}), δ(H−C−C−H) (1237 cm^{-1}), δ(C−H) (1254 cm^{-1}), δ(C−H) (1417 cm^{-1}), and ν(C−C−C−N) (1688 cm^{-1}).

Figure 4c shows the measured SERS spectra from 24 to 32 s. The results show that the peaks at ∼240 and ∼280 cm^{-1} are first replaced by a single peak at ∼243 cm^{-1} and then split into two peaks at the wavenumbers of ∼235 and ∼258 cm^{-1}. The peaks at ∼240 and ∼280 cm^{-1} correspond to the yielded *m*-TS4: 240(δ(mol)) and 283 (δ(mol)) cm^{-1}. The peaks at 235 and 258 cm^{-1} can be assigned to the produced *m*-IM3: 231(δ(mol)) and 264($\delta(mol)_{ip}$) cm^{-1}. These indicate the transition from *m*-TS4 to *m*-IM3. The peaks at ∼554, ∼620, ∼691, ∼774, ∼806, ∼883, ∼986, ∼1024, ∼1242, and ∼1410 cm^{-1} correspond to the vibrations of *m*-TS4: $\delta(C-H)_{ip}$ (561 cm^{-1}), δ(mol (620 cm^{-1})), $\delta(C-H)_{ip}$ (692 cm^{-1}) and δ(C−H) (695 cm^{-1}), δ(H−C−C−H) (775 cm^{-1}), ν(C−H) (i810), $\delta(mol)_{ip}$ (890 cm^{-1}), δ(H−C−C−H) (984 cm^{-1}), δ(mol) (1029 cm^{-1}), δ(H−C−C−H) (1244 cm^{-1}), and δ(H−C−C−H)(1411 cm^{-1}). The peaks at ∼235, ∼258, ∼378, ∼468, ∼611, ∼691, ∼753, ∼774, ∼883, ∼986, ∼1047, ∼1242, and ∼1410 cm^{-1} can be assigned to *m*-IM3: δ(mol) (231 cm^{-1}), $\delta(mol)_{ip}$ (264 cm^{-1}), $\delta(mol)_{oop}$ (372 cm^{-1}), δ(C−C−C−C) (466 cm^{-1}), δ(C−C−C−C) (614 cm^{-1}), δ(mol) (692 cm^{-1}), δ(C−C−C−C−C−N) (742 cm^{-1}), δ(H−C−C−H) (774 cm^{-1}), $\delta(C-C-C-C-C-N)_{ip}$ (889 cm^{-1}), δ(C−C−C−H) (986 cm^{-1}), δ(C−C−C−C) (1035 cm^{-1}), δ(H−C−C−H) (1241 cm^{-1}), and δ(H−C−C−H) (1414 cm^{-1}). The relevant vibration peaks are summarized in Tables S3 and S4, and the corresponding molecular structures are provided in Figure 4d. These results unveil the reaction path CPC → Pyridine → *m*-Pyridyl → Pyridyne → *m*-TS1 → *m*-IM1 → *m*-TS4 → *m*-IM3, which is consistent with the theoretically predicted minimum energy cost route.[18]

Another possible low-cost reaction pathway is *m*-IM1 → *m*-TS2 → *m*-IM2 → *m*-TS3,[18] as shown in Figure S10, and the corresponding peak assignments are summarized in Table S4. Although they share the same reaction products, the measured Raman peaks in our experiments do not match with the calculated ones based on this reaction route. The same analysis was applied to *p*-pyridyl, and the results are summarized in Figure S11 and Table S5. This suggests that *p*-pyridyl could undergo the reaction routes with minimum energy cost: *p*-pyridyl → 3,4-pyridyne → *p*-TS1 → *p*-IM1 → *p*-IM2 → *p*-TS2,[17] as shown in Figure S12, but it could not explain the deviations between the measured Raman peaks and the theoretically predicted ones for both low (200−500 cm^{-1}) and high Raman shift (1000−1800 cm^{-1}) regimes.

Discussion of the Reaction Mechanism. In order to elucidate the role of the yielded hot carriers, the enhancement field, and thermal effect of LSPR, SERS tests were carried out in the reaction with different media. First of all, in order to rule out the possibility of laser carbonization, the power of 785 nm laser beam for Raman measurements was maximized. As shown in Figure S6, the measured spectrum does not indicate any detectable trace of laser carbonization. The SERS test in deionized water indicates two significant new peaks at ∼2084 and ∼2138 cm^{-1} (Figure S13a), indicating the exclusive contributions from the thermal effect, hot carriers, and enhanced field. Recently reported results claim that the environmental temperature change is less than a few tens of K in aqueous solution.[47] However, a contradictory report argues that the local temperature of the plasmonic metal NPs can reach hundreds of K in a liquid medium with significant catalytic effects.[48] Compared to that in the air and N_2, significant carbonization appears in an Ar atmosphere as shown in Figure S13b,c. It can be interpreted as localized sharp temperature rising due to the slow thermal dissipation of argon since it has very low thermal conductivity. This indicates the existence of large amounts of heat during measurements, which also indirectly evidences the thermal contributions in the nonaqueous environment. In other words, the contribution of plasmonic heating is essential. However, we do not obtain any direct evidence to confirm the contributions of hot carriers to the reaction. The adsorbed CPC^+ is susceptible to be attacked by hot electrons to lose its alkyl chain,[34] which indirectly reflects the potential roles of hot electrons in plasmonic catalysis, especially in the initial stage of the reaction. The enhanced field could directly induce electron transfer inside molecules and remarkably enhancement of Raman signals along the field.[20,23] The spectroscopy analysis indicates that the deformation vibration of the molecule is much stronger than stretching vibration, indicating that the field direction is perpendicular to the molecular plane.[49,50] This enlarged deformation vibration could also contribute to the chemical bond broken. Both XPS results and FDTD calculations invoke that the reaction sites are mainly at the edges and corners of the nanoparticles, i.e., hot spot sites that have a stronger enhanced electric field. This also indirectly proves contribution of enhanced field to catalytic effect. In summary, the hot carriers, enhancement field, and thermal effect all contribute to the reaction by varying the reaction barrier.[20−23]

It should be noted that reaction routes are highly dependent on the medium. We have measured the SERS signal of the reaction process in aqueous, N_2, and Ar media, as shown in Figures S14 and S15, and they all show very different reaction

https://doi.org/10.1021/acs.jpcc.1c03760
J. Phys. Chem. C 2021, 125, 18792−18798

pathways. However, more details of each reaction route need to be further investigated.

CONCLUSIONS

In this paper, the ring-opening process of the pyridine head was successfully unveiled through the SERS technique. It reveals the initial formation of pyridyl and pyridine followed by the ring-opening reaction along the route of CPC → Pyridine → *m*-Pyridyl → Pyridyne → *m*-TS1 → *m*-IM1 → *m*-TS4 → *m*-IM3 in the air. This is well explained by the lowest cost reaction pathways predicted by DFT calculations. The reaction is mainly attributed to the LSPR effect, where the locations of reaction sites coincide with the strongly enhanced electric field sites according to FDTD calculations. This demonstrates the applicability of SERS for revealing the pyridine ring-opening type chemical reaction and opens an avenue for its applications to the high-energy cost chemical reaction. Moreover, here, exposed medium-dependent reaction pathways call for more attention for further study.

ASSOCIATED CONTENT

Supporting Information

The Supporting Information is available free of charge at https://pubs.acs.org/doi/10.1021/acs.jpcc.1c03760.

Details of the experimental methods, FDTD and DFT calculations; additional AFM, SEM images; XPS and SERS spectra; FDTD local electric field intensity distribution and DFT calculation results of intermediates; reaction pathways and products; peak assignments of intermediates; Figures S1−S19; and Tables S1−S5 (PDF)

AUTHOR INFORMATION

Corresponding Authors

Yanqing Ma − *Tianjin International Center for Nanoparticles and Nanosystems, Tianjin University, Tianjin 300072, P.R.China; State Laboratory of Precision Measuring Technology and Instruments, Tianjin University, Tianjin 300072, China;* orcid.org/0000-0002-3317-8273; Email: mayanqing@tju.edu.cn

Lei Ma − *Tianjin International Center for Nanoparticles and Nanosystems, Tianjin University, Tianjin 300072, P.R.China;* orcid.org/0000-0002-2446-4833; Email: lei.ma@tju.edu.cn

Authors

Gen Liu − *Tianjin International Center for Nanoparticles and Nanosystems, Tianjin University, Tianjin 300072, P.R.China*

Danni Hao − *Tianjin International Center for Nanoparticles and Nanosystems, Tianjin University, Tianjin 300072, P.R.China*

Kai Wang − *Tianjin International Center for Nanoparticles and Nanosystems, Tianjin University, Tianjin 300072, P.R.China*

Gang Dong − *Tianjin International Center for Nanoparticles and Nanosystems, Tianjin University, Tianjin 300072, P.R.China*

Xue Yu − *Tianjin International Center for Nanoparticles and Nanosystems, Tianjin University, Tianjin 300072, P.R.China*

Rui Xu − *Tianjin International Center for Nanoparticles and Nanosystems, Tianjin University, Tianjin 300072, P.R.China*

Mei Ji − *Tianjin International Center for Nanoparticles and Nanosystems, Tianjin University, Tianjin 300072, P.R.China*

Xiaodong Zhu − *Tianjin International Center for Nanoparticles and Nanosystems, Tianjin University, Tianjin 300072, P.R.China*

Complete contact information is available at: https://pubs.acs.org/10.1021/acs.jpcc.1c03760

Notes

The authors declare no competing financial interest.

ACKNOWLEDGMENTS

This work was financially supported by the National Natural Science Foundation of China (No. 11774255), the National Basic Research Program of China (No. 2020YFC2004602), and the Key Project of Natural Science Foundation of Tianjin City (No. 17JCZDJC30100).

REFERENCES

(1) Kleckley, T. S.; Bennett, J. L.; Wolczanski, P. T.; Lobkovsky, E. B. Pyridine CN Bond Cleavage Mediated by (silox)3Nb (silox = tBu3SiO). *J. Am. Chem. Soc.* **1997**, *119*, 247−248.

(2) Bailey, B. C.; Fan, H.; Huffman, J. C.; Baik, M.-H.; Mindiola, D. J. Room Temperature Ring-Opening Metathesis of Pyridines by a Transient Ti⋮C Linkage. *J. Am. Chem. Soc.* **2006**, *128*, 6798−6799.

(3) Huertos, M. A.; Pérez, J.; Riera, L. Pyridine Ring Opening at Room Temperature at a Rhenium Tricarbonyl Bipyridine Complex. *J. Am. Chem. Soc.* **2008**, *130*, 5662−5663.

(4) Gray, S. D.; Weller, K. J.; Bruck, M. A.; Briggs, P. M.; Wigley, D. E. Carbon-Nitrogen Bond Cleavage in an .eta.2(N,C)-Pyridine Complex Induced by Intramolecular Metal-to-Ligand Alkyl Migration: Models for Hydrodenitrogenation Catalysis. *J. Am. Chem. Soc.* **1995**, *117*, 10678−10693.

(5) Matz, D. L.; Schalnat, M. C.; Pemberton, J. E. Reaction of Thin Films of Solid-State Benzene and Pyridine with Calcium. *J. Am. Chem. Soc.* **2012**, *134*, 12989−12997.

(6) Kasai, P. H.; McLeod, D., Jr. Electron spin resonance study of heterocycles. I. Pyridyl radicals. *J. Am. Chem. Soc.* **1972**, *94*, 720−727.

(7) Solar, S.; Getoff, N.; Sehested, K.; Holcman, J. Pulse radiolysis of pyridine and methylpyridines in aqueous solutions. *Radiat. Phys. Chem.* **1993**, *41*, 825−834.

(8) Turecek, F.; Wolken, J. K.; Sadilek, M. Distinction of Isomeric Pyridyl Cations and Radicals by Neutralization-Reionization Mass Spectrometry, ab Initio and Density Functional Theory Calculations. *Eur. J. Mass Spectrom.* **1998**, *4*, 321−332.

(9) Nam, H. H.; Leroi, G. E. First direct observation of pyridyne: matrix infrared study of the photolysis products of 3,4-pyridinedicarboxylic anhydride. *J. Am. Chem. Soc.* **1988**, *110*, 4096−4097.

(10) Winkler, M.; Cakir, B.; Sander, W. 3,5-PyridyneA Heterocyclic meta-Benzyne Derivative. *J. Am. Chem. Soc.* **2004**, *126*, 6135−6149.

(11) Rau, N. J.; Wenthold, P. G. Experimental Investigation of the Absolute Enthalpies of Formation of 2,3-, 2,4-, and 3,4-Pyridynes. *J. Phys. Chem. A.* **2011**, *115*, 10353−10362.

(12) Shvartsburg, A. A. Aromatic ring destruction in complexes of dipositive metal cations. *Chem. Phys. Lett.* **2003**, *376*, 6−10.

(13) Goetz, A. E.; Garg, N. K. Regioselective reactions of 3,4-pyridynes enabled by the aryne distortion model. *Nat. Chem.* **2013**, *5*, 54−60.

(14) Liu, R.; Huang, T. T. S.; Tittle, J.; Xia, D. A Theoretical Investigation of the Decomposition Mechanism of Pyridyl Radicals. *J. Phys. Chem. A.* **2000**, *104*, 8368−8374.

(15) LaVerne, J. A.; Carmichael, I.; Araos, M. S. Radical Production in the Radiolysis of Liquid Pyridine. *J. Phys. Chem. A.* **2005**, *109*, 461−465.

(16) Cheng, X.; Niu, L.; Zhao, Y.; Zhou, Z. Vibrational analysis for multi-channel decomposition reactions of o-pyridyl radical based on

DFT methods. *Spectrochim. Acta Part A: Mol. Biomol. Spectrosc.* **2004**, *60*, 907−914.
(17) Cheng, X. L.; Zhao, Y. Y.; Zhou, Z. Y. Theoretical studies on p-pyridyl radical decomposition reactions. *J. Mol. Struct.: Theochem.* **2004**, *678*, 17−21.
(18) Cheng, X. Reaction mechanism of decomposition system of m-pyridyl radical: A theoretical investigation. *J. Mol. Struct.: Theochem.* **2005**, *731*, 89−99.
(19) Wu, D. Y.; Ren, B.; Jiang, Y. X.; Xu, X.; Tian, Z. Q. Density Functional Study and Normal-Mode Analysis of the Bindings and Vibrational Frequency Shifts of the Pyridine−M (M = Cu, Ag, Au, Cu +, Ag+, Au+, and Pt) Complexes. *J. Phys. Chem. A.* **2002**, *106*, 9042−9052.
(20) Zhan, C.; Chen, X. J.; Yi, J.; Li, J. F.; Wu, D. Y.; Tian, Z. Q. From plasmon-enhanced molecular spectroscopy to plasmon-mediated chemical reactions. *Nat. Rev. Chem.* **2018**, *2*, 216−230.
(21) Martirez, J. M. P.; Carter, E. A. Prediction of a low-temperature N2 dissociation catalyst exploiting near-IR−to−visible light nanoplasmonics. *Sci. Adv.* **2017**, *3*, No. eaao4710.
(22) Aslam, U.; Rao, V. G.; Chavez, S.; Linic, S. Catalytic conversion of solar to chemical energy on plasmonic metal nanostructures. *Nat. Catal.* **2018**, *1*, 656−665.
(23) Kazuma, E.; Jung, J.; Ueba, H.; Trenary, M.; Kim, Y. Real-space and real-time observation of a plasmon-induced chemical reaction of a single molecule. *Science* **2018**, *360*, 521−526.
(24) Mukherjee, S.; Libisch, F.; Large, N.; Neumann, O.; Brown, L. V.; Cheng, J.; Lassiter, J. B.; Carter, E. A.; Nordlander, P.; Halas, N. J. Hot electrons do the impossible: plasmon-induced dissociation of H2 on Au. *Nano Lett.* **2013**, *13*, 240−247.
(25) Fleischmann, M.; Hendra, P. J.; McQuillan, A. J. Raman spectra of pyridine adsorbed at a silver electrode. *Chem. Phys. Lett.* **1974**, *26*, 163−166.
(26) Albrecht, M. G.; Creighton, J. A. Anomalously intense Raman spectra of pyridine at a silver electrode. *J. Am. Chem. Soc.* **1977**, *99*, 5215−5217.
(27) Szczerbiński, J.; Gyr, L.; Kaeslin, J.; Zenobi, R. Plasmon-Driven Photocatalysis Leads to Products Known from E-beam and X-ray-Induced Surface Chemistry. *Nano Lett.* **2018**, *18*, 6740−6749.
(28) Wang, Y. H.; Wei, J.; Radjenovic, P.; Tian, Z. Q.; Li, J. F. In Situ Analysis of Surface Catalytic Reactions Using Shell-Isolated Nanoparticle-Enhanced Raman Spectroscopy. *Anal. Chem.* **2019**, *91*, 1675−1685.
(29) Dong, J. C.; Zhang, X. G.; Briega-Martos, V.; Jin, X.; Yang, J.; Chen, S.; Yang, Z. L.; Wu, D. Y.; Feliu, J. M.; Williams, C. T.; Tian, Z. Q.; Li, J. F. In situ Raman spectroscopic evidence for oxygen reduction reaction intermediates at platinum single-crystal surfaces. *Nat. Energy* **2019**, *4*, 60−67.
(30) Zhan, C.; Wang, Z. Y.; Zhang, X. G.; Chen, X. J.; Huang, Y. F.; Hu, S.; Li, J. F.; Wu, D. Y.; Moskovits, M.; Tian, Z. Q. Interfacial Construction of Plasmonic Nanostructures for the Utilization of the Plasmon-Excited Electrons and Holes. *J. Am. Chem. Soc.* **2019**, *141*, 8053−8057.
(31) Zhao; Jensen, L.; Schatz, G. C. Pyridine−Ag20 Cluster: A Model System for Studying Surface-Enhanced Raman Scattering. *J. Am. Chem. Soc.* **2006**, *128*, 2911−2919.
(32) Li, J. F.; Ding, S. Y.; Yang, Z. L.; Bai, M. L.; Anema, J. R.; Wang, X.; Wang, A.; Wu, D. Y.; Ren, B.; Hou, S. M.; Wandlowski, T.; Tian, Z. Q. Extraordinary Enhancement of Raman Scattering from Pyridine on Single Crystal Au and Pt Electrodes by Shell-Isolated Au Nanoparticles. *J. Am. Chem. Soc.* **2011**, *133*, 15922−15925.
(33) Domke, K. F.; Zhang, D.; Pettinger, B. Enhanced Raman Spectroscopy: Single Molecules or Carbon? *J. Phys. Chem. C* **2007**, *111*, 8611−8616.
(34) Brooks, J. L.; Warkentin, C. L.; Chulhai, D. V.; Goodpaster, J. D.; Frontiera, R. R. Plasmon-Mediated Intramolecular Methyl Migration with Nanoscale Spatial Control. *ACS Nano* **2020**, *14*, 17194−17202.
(35) Tao, A. R.; Ceperley, D. P.; Sinsermsuksakul, P.; Neureuther, A. R.; Yang, P. Self-Organized Silver Nanoparticles for Three-Dimensional Plasmonic Crystals. *Nano Lett.* **2008**, *8*, 4033−4038.
(36) Rycenga, M.; Cobley, C. M.; Zeng, J.; Li, W.; Moran, C. H.; Zhang, Q.; Qin, D.; Xia, Y. Controlling the Synthesis and Assembly of Silver Nanostructures for Plasmonic Applications. *Chem. Rev.* **2011**, *111*, 3669−3712.
(37) Link, S.; El-Sayed, M. A. Spectral Properties and Relaxation Dynamics of Surface Plasmon Electronic Oscillations in Gold and Silver Nanodots and Nanorods. *J. Phys. Chem. B* **1999**, *103*, 8410−8426.
(38) El-Sayed, M. A. Some Interesting Properties of Metals Confined in Time and Nanometer Space of Different Shapes. *Acc. Chem. Res.* **2001**, *34*, 257−264.
(39) Boerigter, C.; Campana, R.; Morabito, M.; Linic, S. Evidence and implications of direct charge excitation as the dominant mechanism in plasmon-mediated photocatalysis. *Nat. Commun.* **2016**, *7*, 10545.
(40) Sun, S.; Birke, R. L.; Lombardi, J. R. Surface-enhanced Raman spectroscopy of surfactants on silver electrodes. *J. Phys. Chem.* **1990**, *94*, 2005−2010.
(41) Koglin, E.; Kip, B. J.; Meier, R. J. Adsorption and Displacement of Melamine at the Ag/Electrolyte Interface Probed by Surface-Enhanced Raman Microprobe Spectroscopy. *J. Phys. Chem.* **1996**, *100*, 5078−5089.
(42) Liu, H.; Lin, D.; Sun, Y.; Yang, L.; Liu, J. Cetylpyridinium Chloride Activated Trinitrotoluene Explosive Lights Up Robust and Ultrahigh Surface-Enhanced Resonance Raman Scattering in a Silver Sol. *Chem. − Eur. J.* **2013**, *19*, 8789−8796.
(43) Maksymovych, P.; Sorescu, D. C.; Yates, J. T. Gold-Adatom-Mediated Bonding in Self-Assembled Short-Chain Alkanethiolate Species on the Au(111) Surface. *Phys. Rev. Lett.* **2006**, *97*, No. 146103.
(44) Jacobs, M. B.; Jagodzinski, P. W.; Jones, T. E.; Eberhart, M. E. A Surfaced-Enhanced Raman Spectroscopy and Density Functional Theory Study of [Au(CN)2]−/[Au(CN)4]− Adsorbed on Gold Nanoparticles. *J. Phys. Chem. C* **2011**, *115*, 24115−24122.
(45) Zhong, J. H.; Jin, X.; Meng, L.; Wang, X.; Su, H. S.; Yang, Z. L.; Williams, C. T.; Ren, B. Probing the electronic and catalytic properties of a bimetallic surface with 3 nm resolution. *Nat. Nanotechnol.* **2017**, *12*, 132−136.
(46) Eesley, G. L.; Burkstrand, J. M. X-ray-photoemission and Raman spectroscopy investigation of pyridine on Ag. *Phys. Rev. B* **1981**, *24*, 582−585.
(47) Pensa, E.; Gargiulo, J.; Lauri, A.; Schlücker, S.; Cortés, E.; Maier, S. A. Spectral Screening of the Energy of Hot Holes over a Particle Plasmon Resonance. *Nano Lett.* **2019**, *19*, 1867−1874.
(48) Adleman, J. R.; Boyd, D. A.; Goodwin, D. G.; Psaltis, D. Heterogenous Catalysis Mediated by Plasmon Heating. *Nano Lett.* **2009**, *9*, 4417−4423.
(49) Ding, S. Y.; You, E.-M.; Tian, Z. Q.; Moskovits, M. Electromagnetic theories of surface-enhanced Raman spectroscopy. *Chem. Soc. Rev.* **2017**, *46*, 4042−4076.
(50) Xu, H.; Bjerneld, E. J.; Käll, M.; Börjesson, L. Spectroscopy of Single Hemoglobin Molecules by Surface Enhanced Raman Scattering. *Phys. Rev. Lett.* **1999**, *83*, 4357−4360.

https://doi.org/10.1021/acs.jpcc.1c03760
J. Phys. Chem. C 2021, 125, 18792−18798